Journal of Biomedical Optics

BiomedicalOptics.SPIEDigitalLibrary.org

Photoacoustic tomography of vascular compliance in humans

Pengfei Hai
Yong Zhou
Jinyang Liang
Chiye Li
Lihong V. Wang

SPIE.

Journal of Biomedical Optics 20(12), 126008 (December 2015)

Photoacoustic tomography of vascular compliance in humans

Pengfei Hai,[†] Yong Zhou,[†] Jinyang Liang, Chiye Li, and Lihong V. Wang[*]
Washington University in St. Louis, Department of Biomedical Engineering, Optical Imaging Laboratory, One Brookings Drive, St. Louis, Missouri 63130, United States

Abstract. Characterization of blood vessel elastic properties can help in detecting thrombosis and preventing life-threatening conditions such as acute myocardial infarction or stroke. Vascular elastic photoacoustic tomography (VE-PAT) is proposed to measure blood vessel compliance in humans. Implemented on a linear-array-based photoacoustic computed tomography system, VE-PAT can quantify blood vessel compliance changes due to simulated thrombosis and occlusion. The feasibility of the VE-PAT system was first demonstrated by measuring the strains under uniaxial loading in perfused blood vessel phantoms and quantifying their compliance changes due to the simulated thrombosis. The VE-PAT system detected a decrease in the compliances of blood vessel phantoms with simulated thrombosis, which was validated by a standard compression test. The VE-PAT system was then applied to assess blood vessel compliance in a human subject. Experimental results showed a decrease in compliance when an occlusion occurred downstream from the measurement point in the blood vessels, demonstrating VE-PAT's potential for clinical thrombosis detection. [DOI: 10.1117/1.JBO.20.12.126008]

Keywords: photoacoustic tomography; vascular elasticity; vascular compliance; thrombosis.

Paper 150611R received Sep. 11, 2015; accepted for publication Nov. 19, 2015; published online Dec. 21, 2015.

1 Introduction

Mechanical properties of biological tissue are directly related to its underlying structure and can be altered by pathological states such as tumors and arteriosclerosis. Particularly, the elastic properties of blood vessels are strongly affected by hemodynamic changes in the circulation system and may indicate the presence of thrombosis and vessel occlusion, which can lead to severe conditions such as stroke, acute heart attack, and pulmonary embolism.[1,2] Partially or fully clogged blood vessels under thrombosis are usually harder to compress.[2] Thus, characterizing the elastic properties of blood vessels under different hemodynamic states can potentially contribute to the detection of thrombosis and help prevent it from developing into acute life-threatening conditions.

Inspired by manual palpation, medical imaging technologies have been applied to image the elastic properties of biological tissue.[3] By measuring the tissue's deformation under loading, elasticity imaging techniques usually map the mechanical properties of biological tissue onto an image called an elastogram. An elastogram conveys the local variations of stiffness in the region of interest and adds a new dimension of information that may help clinical diagnosis and therapy. In addition to its primary application in breast cancer diagnosis, elasticity imaging techniques also find applications in blood vessel stiffness characterization.[4,5] Vascular elasticity imaging was first implemented invasively by using endovascular imaging catheters.[6,7] Based on various imaging modalities, noninvasive vascular elasticity imaging was later achieved, including ultrasound elastography (USE), magnetic resonance elastography (MRE), and optical coherence elastography (OCE).[8–10] USE can image blood vessels in deep regions, but the poor ultrasonic scattering contrast between blood and extravascular tissue makes it insensitive to the deformations of small blood vessels.[11] MRE can potentially penetrate the whole human body, but its spatial resolution (~1 to 3 mm) is sufficient for assessing the stiffness of large blood vessels only.[12] Benefiting from the high spatial resolution of optical coherence tomography, OCE has a typical spatial resolution of 1 to 10 μm and can detect displacement at the submicrometer level. Thus it is capable of mapping small blood vessel elasticity.[13] However, OCE suffers from strong optical scattering in biological tissue, limiting its penetration depth to ~1 mm, which is insufficient for assessing elastic properties of blood vessels in the optical diffusive regime in tissues.

Combining optical excitation with acoustic detection, photoacoustic tomography (PAT) provides high spatial resolution at depth with high detection sensitivity.[14] With strong optical absorption contrast provided by hemoglobin in red blood cells, PAT has achieved structural and functional imaging of vasculature in both animals and humans.[15–17] PAT has also been applied to measure the elastic properties of biological tissue *ex vivo*.[18] However, by measuring the phase delay between the dominant frequency photoacoustic wave and the reference signal, the current photoacoustic technique is able to detect only the viscosity–elasticity ratio instead of the elasticity, which is not applicable to assess the vascular elastic properties in humans *in vivo*.[18]

In this work, we report noninvasive vascular elastic photoacoustic tomography (VE-PAT), capable of measuring blood vessel compliance changes at depth in humans. Because PAT is highly sensitive to blood, the term "blood vessel" in this work specifically refers to blood perfused vessels. By measuring the compliance changes of blood vessel phantoms with and without simulated thrombosis, we demonstrated the feasibility of VE-PAT in characterizing blood vessel elasticity. We further

*Address all correspondence to: Lihong V. Wang, E-mail: lhwang@wustl.edu

†These authors contributed equally to this work.

1083-3668/2015/$25.00

applied this technique to humans and detected a decrease of blood vessel compliance after downstream vessel occlusion, demonstrating the potential of VE-PAT in clinical thrombosis detection.

2 Materials and Methods

2.1 *Experimental System*

In VE-PAT, the major device is a linear-array-based photoacoustic imaging probe.[19,20] The probe used here consisted of a linear array ultrasonic transducer (Visualsonics Inc. LZ250, 21 MHz center frequency, 78% one-way bandwidth, 256 elements, 23 × 3 mm array size) with two optical fiber bundle strips (20 × 1.25 mm) mounted on each side [Fig. 1(a)]. The laser beams coming out of the two optical fiber bundle strips had an angle of incidence of 30 deg with respect to the imaging plane. The two optical fiber bundles were bifurcated from a single optical bundle that was incorporated into the probe together with an ultrasound signal cable. A tunable optical parametric oscillator laser (680 to 970 nm, 20-Hz pulse repetition rate) was coupled into the single fiber optical bundle for photoacoustic excitation. The wavelength was set to 850 nm to achieve deep penetration for vascular elasticity imaging. In our experiments, the fluence on the sample surface was 10 mJ/cm^2, well within the safety limit set by the American National Standards Institute (20 mJ/cm^2). Each element of the transducer array was cylindrically focused with a focal length of 15 mm. For each of four laser pulses, photoacoustic signals were captured sequentially on one quarter (i.e., 64 elements) of the transducer array elements. After all data were acquired from the four segments, we reconstructed a two-dimensional (2-D) photoacoustic image using the filtered back-projection algorithm.[21] The reconstructed 2-D photoacoustic image is referred to hereafter as the B-scan photoacoustic image. An imaging station (Vevo LAZR, Visualsonics Inc.) displayed the reconstructed B-scan photoacoustic images at 5 frames/s, as determined by the 20 Hz laser repetition rate and the four-to-one multiplexing in the image acquisition system. The VE-PAT system has spatial resolutions of 119 μm in the lateral direction, 86 μm in the axial direction, and 1237 μm in the elevational direction.[20] The minimum displacement that can be resolved is 18.3 μm, which is determined by the data acquisition sampling rate of 84 MHz and the average speed of sound in biological tissue of 1540 m/s. The typical signal-to-noise ratios of the VE-PAT system were around 25 dB in the following phantom experiments and 20 dB in the *in vivo* experiments in humans.

To implement VE-PAT, a customized compression stage was developed and incorporated into the probe. The compression stage had an aluminum plate controlled by a three-dimensional translation stage, which could position the plate in the $x-y$ plane and induce precise displacements along the z axis for accurate sample compression [Fig. 1(b)]. Above the compression plate, a water tank held water for acoustic coupling. An imaging window slightly larger than the probe was machined in the center of the compression plate. To ensure the compression force applied to the sample was normal and uniaxial, a piece of fully stretched polymethylpentene plastic membrane was attached to the bottom of the compression plate, which allowed the transmission of both the optical excitation light and the generated photoacoustic wave. An aluminum block on an optical table held the sample against compression.

2.2 *Phantom Preparation*

Silicone microtubes with 0.3 mm (60985-700, VWR) and 3.4 mm inner diameters (60985-720, VWR) perfused with bovine blood (905, Quad-Five) mimicked small and large blood vessels, respectively. Blood was pumped into the microtubes through a syringe, and the flow speed was controlled by a syringe pump (BSP-99M, Braintree Scientific). The thrombosis was simulated by injecting a small drop of glue into the microtube downstream from the measurement point, which hardened on the tube wall and partially blocked the flow. The microtube was then embedded in tissue-mimicking gelatin phantoms 3 mm deep [Fig. 2(a)]. To achieve stiffness similar to that of soft tissue, the gelatin concentration in the phantoms was 100 g/L.[22] To achieve similar optical scattering as in biological tissue, 1% intralipid was added to the gelatin phantoms.

2.3 *Method*

2.3.1 *Sample compression and photoacoustic image acquisition*

Elastic property changes induced by simulated thrombosis were investigated in both the large and small blood vessel phantoms. As shown in Fig. 1(b), the axis of the phantom blood vessel was perpendicular to the imaging plane. A cross section of the phantom was first imaged right after the compression plate contacted

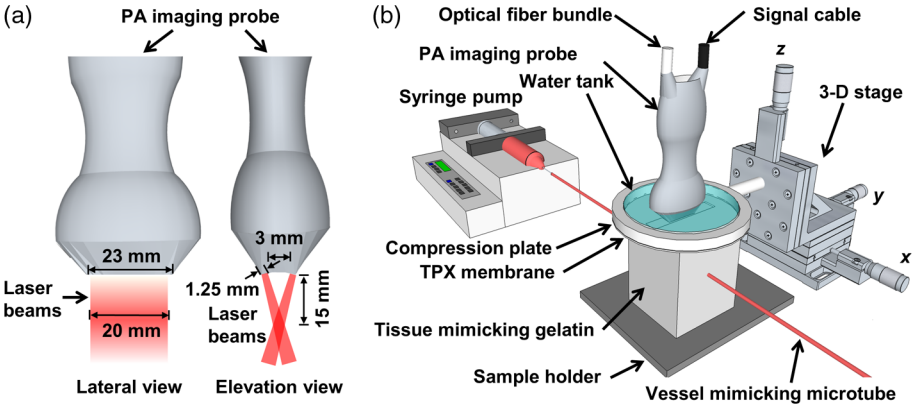

Fig. 1 Schematic of vascular elastic photoacoustic tomography (VE-PAT): (a) photoacoustic imaging probe and (b) VE-PAT setup for a blood vessel phantom imaging. The imaging probe is incorporated with a customized compression stage.

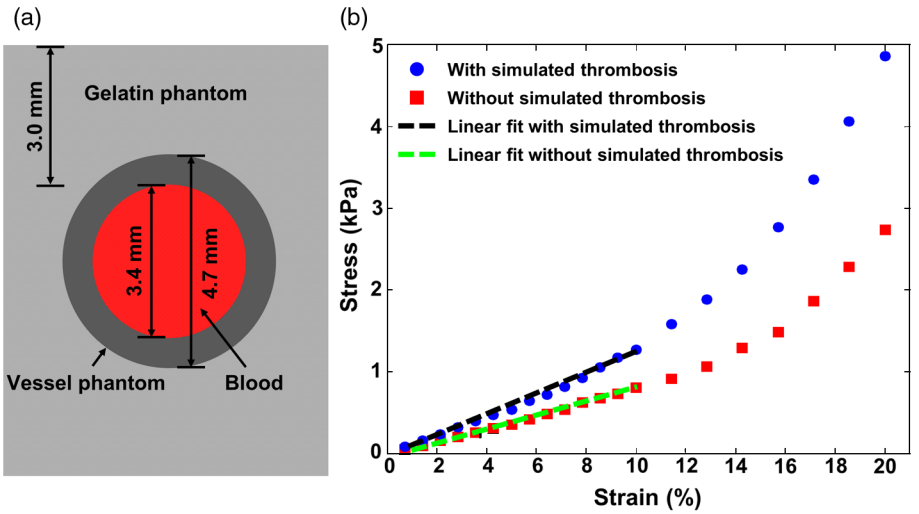

Fig. 2 Characterization of a large blood vessel phantom: (a) diagram of the large blood vessel phantom embedded 3 mm deep in gelatin and (b) stress–strain response measured for the large blood vessel phantom with and without simulated thrombosis. Stress–strain curves with strain smaller than 10% were fitted to linear functions to calculate the compliances as shown by the dashed lines.

the sample with a minimum load. For the big vessel (ID = 3.4 mm), we applied 10 small steps of compression with a step size of 50 μm and two large steps of compression with a step size of 500 μm. For the small vessel phantom (ID = 0.3 mm), only one 50 μm step compression was applied instead of 12 steps. For all the compression steps, corresponding photoacoustic images were acquired when the phantom had stabilized. The same compression and imaging procedure was performed in both conditions, with and without simulated thrombosis.

In vivo blood vessel elasticity was assessed on the middle finger of the right hand of a 29-year-old male volunteer. All of the experiments were conducted in accordance with the human studies protocols approved by the Institutional Review Board at Washington University in St. Louis. The right hand was placed on the object holder, and the middle finger was fixed in position and imaged by the VE-PAT system. Similar to the procedures in our phantom experiments, a cross section of the finger was first imaged just after the compression plate contacted the finger with a minimum load. Then we applied five small steps of compression with a step size of 50 μm and two large steps of compression with a step size of 300 μm. Photoacoustic images were acquired after each step of compression. To simulate thrombosis, a vessel occlusion was created on the near end of the middle finger. The same compression and imaging procedure were repeated to obtain the elastic property changes of a finger vessel due to the occlusion. The occlusion time was short enough (60 s) to avoid any potential harm.

2.3.2 *Strain calculation*

Strain values of the blood vessel phantoms and the finger blood vessels under compression were obtained via analyzing the reconstructed B-scan photoacoustic images before and after compression based on the following method. First, the photoacoustic images at preload were segmented based on a threshold of 6 dB with respect to the noise level, and the original distances L between the top and bottom boundaries of the blood vessels were calculated at each reconstructed A-line. Then, corresponding reconstructed A-lines in the photoacoustic images before and after compression were analyzed with a sliding window cross-correlation method.[3] The sliding window was set slightly larger than the visible vessel boundaries in the photoacoustic images. By doing cross correlation between the corresponding signals within the window before and after compression, axial displacements of the top and bottom boundaries, denoted as d_t and d_b, were estimated. The strain ε was then calculated by

$$\varepsilon = \frac{d_t - d_b}{L}. \tag{1}$$

As the compliance C is proportional to the strain ε, the ratio of the compliances C_1 and C_2 of two samples under the same stress equals the ratio of their strains ε_1 and ε_2:

$$\frac{C_1}{C_2} = \frac{\varepsilon_1}{\varepsilon_2}. \tag{2}$$

3 Results

3.1 *Standard Compression Test of the Large Blood Vessel Phantom*

Before the microtubes were embedded into tissue-mimicking gelatin phantoms, the compliances of the perfused large blood vessel phantoms with and without simulated thrombosis were measured with a standard compression test. In the standard compression test, the large blood vessel phantom was placed on a high-precision digital weighing scale (S200, Ohaus) and compressed using the customized compression stage. The compression stress was calculated based on the difference in the scale readings before and after compression. The axial displacement of the top boundary was read from the translation stage that moved the compression plate along the z axis for precise sample compression. Because the bottom boundary did not move, the strain was calculated as the deformation over the original diameter of the blood vessel phantom [Eq. (1)]. Consistent with the

previous elasticity imaging studies,[23] the strain–stress relationship appeared linear with the coefficient of determination (R^2) of 0.993 and 0.987 when the strain was smaller than 10% [Fig. 2(b)]. The ratio of the compliances between cases with and without simulated thrombosis was 0.64.

3.2 *Vascular Elastic Photoacoustic Tomography of Large Blood Vessel Phantom*

Photoacoustic images of a cross section of the large blood vessel phantom before and after 10 small steps of compression with a step size of 50 μm are shown in Fig. 3. The diameter of the large blood vessel phantom before compression was measured to be 3513.6 μm. The axial displacements of the top and bottom boundaries and the strain values of the large blood vessel phantom are summarized in Table 1. Under the same stress, the blood vessel phantom without simulated thrombosis [Figs. 3(a) and 3(b)] underwent larger deformation than that with simulated thrombosis [Figs. 3(c) and 3(d)]. The strain values of the large blood vessel phantom with and without simulated thrombosis were plotted at each compression step [Fig. 3(i)]. During the 10 small steps of compression, the strain–stress response still appeared linear, as shown in Fig. 3(i). We quantified the relative compliance by fitting the two data sets to linear functions. The compliance ratio between the two states was estimated to be 0.67, which is close to the ratio of 0.64 measured in the standard compression test.

Figures 3(e)–3(h) show B-scan photoacoustic images of a cross section of the large blood vessel phantom before and after two large steps of compression with a step size of 500 μm, during which the strain reached the apparent nonlinear strain–stress response regime. The blood vessel phantom became harder to compress in the presence of simulated thrombosis [Figs. 3(g)–3(h)], akin to the linear strain–stress response result. The strain values at the first compression state for the blood vessel phantom with and without simulated thrombosis were $12.9\% \pm 1.3\%$ and $16.3\% \pm 1.1\%$, respectively. At the second compression state, they were $15.8\% \pm 1.4\%$ and $22.4\% \pm 1.7\%$, respectively [Fig. 3(i)]. Since the same compression forces were applied to the blood vessel phantom with and without simulated thrombosis at each state, the smaller strains

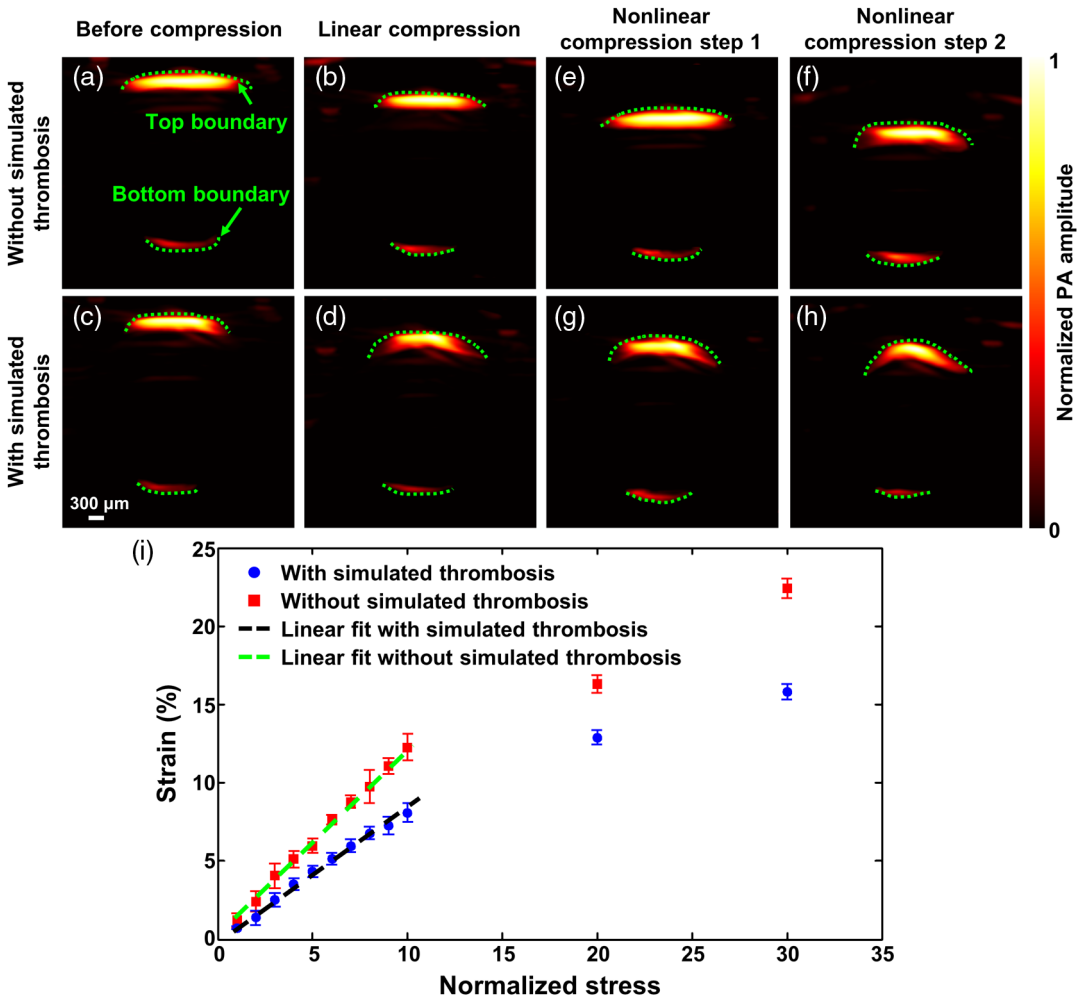

Fig. 3 VE-PAT of a large blood vessel phantom. Photoacoustic images of a cross section in the large blood vessel phantom without thrombosis (a) before and (b) after 10 small steps of compression, and (e)–(f) after two large steps of compression. Photoacoustic images of the cross section in the large blood vessel phantom with simulated thrombosis (c) before, (d) after 10 small steps of compression, and (g)–(h) after two large steps of compression. (i) Strain curves under 12 steps of compression for the large blood vessel phantom with and without simulated thrombosis. Dashed lines: linear fits with the coefficient of determination (R^2) of 0.998 and 0.995 for $\leq$13% strain. Error bars: standard deviation.

Table 1 Vascular elastic photoacoustic tomography (VE-PAT) of axial displacements and strains of the large blood vessel phantom. The linear compression is the result from 10 total compression steps.

		Linear compression	Nonlinear compression step 1	Nonlinear compression step 2
Without thrombosis	Top boundary displacement (μm)	475.8	732.0	1006.5
	Bottom boundary displacement (μm)	43.9	161.0	219.6
	Deformation (μm)	431.9	571.0	786.9
	Strain (%)	12.3	16.3	22.4
	Standard deviation of strain (%)	0.9	1.1	1.7
With thrombosis	Top boundary displacement (μm)	320.3	567.3	695.4
	Bottom boundary displacement (μm)	34.8	113.4	139
	Deformation (μm)	285.5	453.9	556.4
	Strain (%)	8.1	12.9	15.8
	Standard deviation of strain (%)	0.6	1.3	1.4

indicated that a decrease in compliance of the blood vessel phantom was induced by the simulated thrombosis.

3.3 *Vascular Elastic Photoacoustic Tomography of Small Blood Vessel Phantom*

Photoacoustic images of a cross section of the small blood vessel were acquired before and after compression with and without simulated thrombosis [Figs. 4(a)–4(d)]. The diameter of the small blood vessel phantom before compression was measured to be 329.4 μm. The axial displacements of the top and bottom boundaries and the strain values of the small blood vessel phantom are summarized in Table 2. Similar to the large blood vessel phantom, the small blood vessel phantom was harder to compress with the simulated thrombosis. The strain for the small blood vessel phantom without simulated thrombosis was $13.3 \pm 0.9\%$ while the strain with simulated thrombosis was only $6.7\% \pm 0.4\%$ [Fig. 4(e)]. Under the same compression force, the decrease in strain indicated a decrease in compliance due to the simulated thrombosis.

3.4 *Vascular Elastic Photoacoustic Tomography of Blood Vessels in a Human*

Figure 5 shows the VE-PAT results of the middle finger blood vessels of the human subject with and without vessel

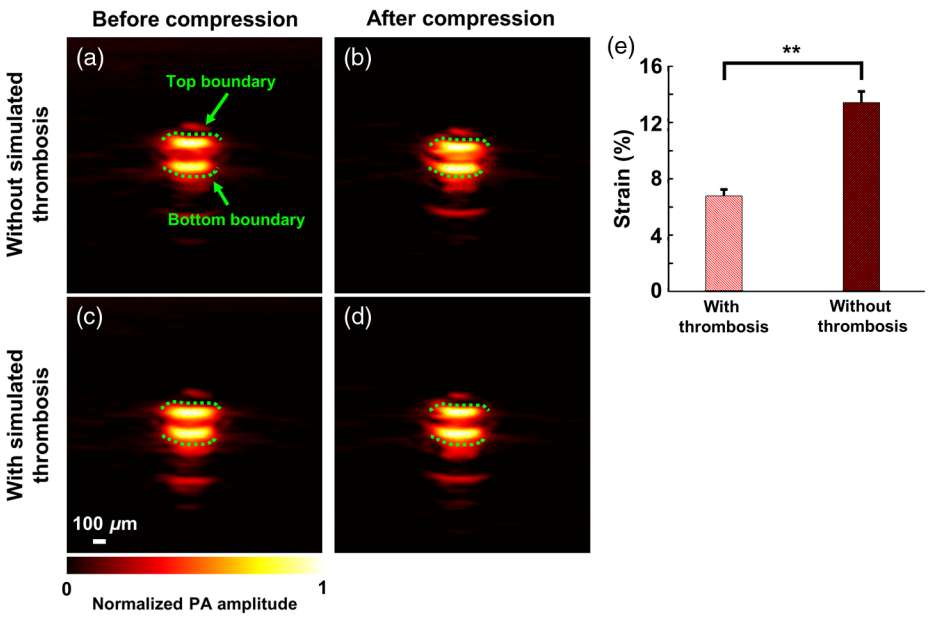

Fig. 4 VE-PAT of a small blood vessel phantom. Photoacoustic images of a cross section of the small blood vessel phantom without simulated thrombosis (a) before and (b) after compression, with simulated thrombosis (c) before and (d) after compression. (e) Strain values for the small blood vessel phantom with and without thrombosis. Statistics: paired Student's *t*-test. *P* values: **<0.05.

Table 2 VE-PAT of axial displacements and strains of the small blood vessel phantom.

	Without thrombosis	With thrombosis
Top boundary displacement (μm)	71.4	45.8
Bottom boundary displacement (μm)	27.5	23.8
Deformation (μm)	43.9	22.0
Strain (%)	13.3	6.7
Standard deviation of strain (%)	0.9	0.4

occlusion. The diameter of the blood vessel in the human finger before compression was measured to be 786.9 μm. The axial displacements of the top and bottom boundaries and the strain values of the finger blood vessel are summarized in Table 3. During five small steps of compression with a step size of 50 μm, the blood vessel in the finger underwent smaller deformation with vessel occlusion downstream [Figs. 5(a)–5(d)]. Strain values for the blood vessels at each step of compression were calculated for both normal and vessel occlusion conditions [Fig. 5(e)]. Since the largest deformation was still within the linear strain–stress response regime, we estimated a relative decrease of compliance as 30.0% when the vessel was occluded.

The finger was then compressed with two 300 μm steps, during which the blood vessels underwent larger deformation so that the strain–stress response became nonlinear

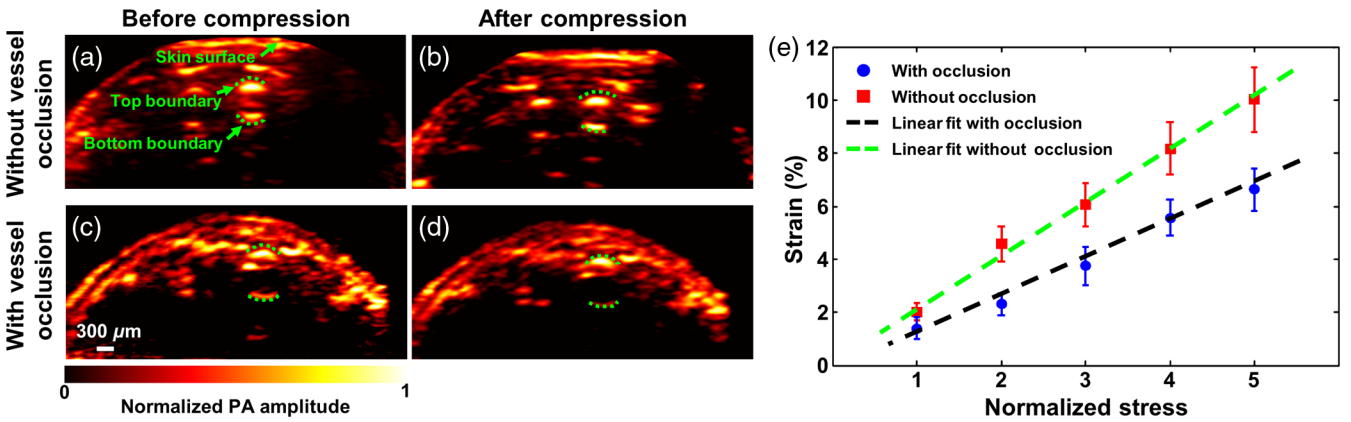

Fig. 5 VE-PAT of a human finger in the linear strain–stress response regime. Photoacoustic images of a cross section of the human finger without vessel occlusion (a) before and (b) after compression and with vessel occlusion (c) before and (d) after compression. (e) Strain curves under five steps of compression for the human finger with and without vessel occlusion. Dashed lines: linear fits with the coefficient of determination (R^2) of 0.993 and 0.987. Error bars: standard deviation.

Table 3 VE-PAT of axial displacements and strains of the human finger blood vessel *in vivo*. The linear compression is the result from five total compression steps.

		Linear compression	Nonlinear compression step 1	Nonlinear compression step 2
Without vessel occlusion	Top boundary displacement (μm)	234.2	456.1	585.6
	Bottom boundary displacement (μm)	155.5	161.0	208.7
	Deformation (μm)	78.7	295.1	376.9
	Strain (%)	10.0	37.5	47.9
	Standard deviation of strain (%)	2.8	5.8	6.1
With vessel occlusion	Top boundary displacement (μm)	165.6	259.9	475.7
	Bottom boundary displacement (μm)	113.4	128.1	295.5
	Deformation (μm)	52.2	131.8	180.2
	Strain (%)	6.6	16.7	22.9
	Standard deviation of strain (%)	0.8	3.4	4.5

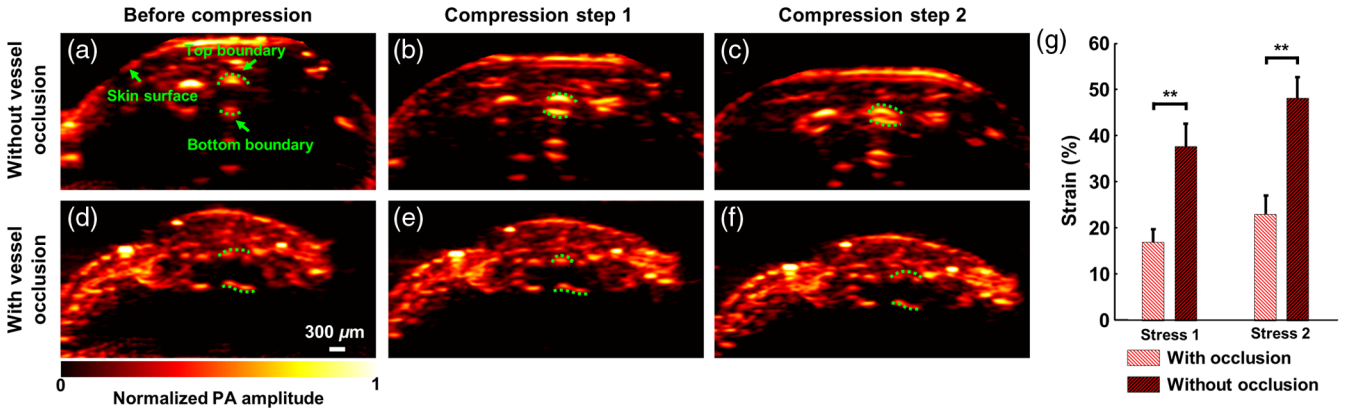

Fig. 6 VE-PAT of a human finger in the nonlinear strain–stress response regime. Photoacoustic images of a cross section of the human finger without vessel occlusion (a) before compression, (b) after compression step 1, and (c) after compression step 2. Photoacoustic images of the same cross section of the human finger with vessel occlusion (d) before compression, (e) after compression step 1, and (f) after compression step 2. (g) Strain values for the blood vessels with and without thrombosis in two compression steps. Statistics: paired Student's *t*-test. *P* values: **<0.05.

[Figs. 6(a)–6(f)]. Again, the blood vessels with occlusion underwent smaller deformation than that without occlusion under the same load. Strain values for blood vessels without occlusion at the two steps were $37.5\% \pm 5.8\%$ and $47.9\% \pm 6.1\%$, while they were $16.7\% \pm 3.4\%$ and $22.9\% \pm 4.5\%$ with vessel occlusion [Fig. 6(g)]. These results demonstrated that VE-PAT can detect the decrease of vessel compliance in the human finger due to vessel occlusion in both the linear and nonlinear strain–stress response regimes.

4 Discussions and Conclusions

By incorporating a linear-array-based photoacoustic imaging probe with a customized compression stage, we have developed VE-PAT that can detect blood vessel elasticity changes due to abnormal hemodynamic states. VE-PAT detected vascular compliance changes due to simulated thrombosis in large and small blood vessel phantoms at depths and in blood vessels in a finger of a human subject *in vivo*. In the large blood vessel phantom, the compliance ratio between the two states with and without simulated thrombosis measured by VE-PAT agreed with the value measured in the standard compression test. By imaging the small blood vessel phantom embedded 3 mm deep in the gelatin phantom, VE-PAT demonstrated its capability to detect elasticity changes of small blood vessels at depths that are difficult for either USE or OCE to image. In addition, VE-PAT was applied to assess blood vessel elasticity changes due to vessel occlusion in the human finger, demonstrating its potential for clinical vessel elasticity characterization.

The detection sensitivity of the VE-PAT system is limited by the minimum detectable displacement, that is, 18.3 μm. First, the minimum detectable displacement limits the minimum diameter of blood vessels whose elasticity can be assessed by VE-PAT in the linear strain–stress response regime, which is usually considered to be less than 10% strain in biological tissue. To stay within the linear strain–stress response regime, the blood vessel diameter should be at least 183 μm, that is, 10 times (reciprocal of 10%) the minimum detectable displacement. For blood vessels with diameters smaller than 183 μm and larger than the minimum detectable displacement of 18.3 μm, their elasticity can still be assessed, but only in the nonlinear stress–strain response regime. For blood vessels with diameters smaller than 18.3 μm, their deformation cannot be resolved, which is the ultimate detection limit of the current VE-PAT system.

To the best of our knowledge, this is the first time that PAT has been applied for quantitative assessment of blood vessel elastic properties in humans *in vivo*. In addition to the information that photoacoustic imaging can provide including structure, flow velocity, molecule concentration, and oxygen saturation level of hemoglobin,[24–27] VE-PAT adds important elasticity information. VE-PAT has potential for use in many clinical applications, including detection of deep venous thrombosis, characterization of vulnerable plaque, and evaluation of atherosclerotic tissues.

Acknowledgments

We thank Alejandro Garcia-Uribe for his assistance in human experiments and Professor James Ballard for a close reading of this paper. This work was sponsored by the National Institutes of Health Grants DP1 EB016986 (NIH Director's Pioneer Award), R01 CA186567 (NIH Director's Transformative Research Award), and S10 RR026922. L. V. Wang has a financial interest in Endra, Inc., and Microphotoacoustics, Inc., which, however, did not support this work.

References

1. C. Pasterkamp and E. Falk, "Atherosclerotic plaque rupture: an overview," *J. Clin. Basic Cardiol.* **3**(2), 81–86 (2000).
2. S. Emelianov, X. Chen, and M. O'Donnell, "Triplex ultrasound: elasticity imaging to age deep venous thrombosis," *Ultrasound Med. Biol.* **28**(6), 757–767 (2002).
3. J. Ophir et al., "Elastography: a quantitative method for imaging the elasticity of biological tissues," *Ultrason. Imaging* **13**(2), 111–134 (1991).
4. A. Goddi, M. Bonardi, and S. Alessi, "Breast elastography: a literature review," *J. Ultrasound* **15**(3), 192–198 (2012).
5. C. L. de Korte and A. F. W. van der Steen, "Intravascular ultrasound elastography: an overview," *Ultrasonics* **40**(1–8), 859–865 (2002).
6. C. L. de Korte et al., "Characterization of plaque components and vulnerability with intravascular ultrasound elastography," *Phys. Med. Biol.* **45**(6), 1465–1475 (2000).

7. G. van Soest et al., "Robust intravascular optical coherence elastography by line correlations," *Phys. Med. Biol.* **52**(9), 2445–2458 (2007).
8. C. Schmitt et al., "Noninvasive vascular elastography: toward a complementary characterization tool of atherosclerosis in carotid arteries," *Ultrasound Med. Biol.* **33**(12), 1841–1858 (2007).
9. D. A. Woodrum, "A phase-contrast MRI-based elastography technique detects early hypertensive changes in ex-vivo porcine aortic wall," *J. Magn. Reson. Imaging* **29**(3), 583–587 (2009).
10. J. Rogowska et al., "Quantitative optical coherence tomographic elastography: method for assessing arterial mechanical properties," *Br. J. Radiol.* **79**(945), 707–711 (2006).
11. R. Righetti, S. Srinivasan, and J. Ophir, "Lateral resolution in elastography," *Ultrasound Med. Biol.* **29**(5), 695–704 (2003).
12. A. Manduca et al., "Magnetic resonance elastography: non-invasive mapping of tissue elasticity," *Med. Image Anal.* **5**(4), 237–254 (2001).
13. C. Sun, B. Standish, and V. X. D. Yang, "Optical coherence elastography: current status and future applications," *J. Biomed. Opt.* **16**(4), 043001 (2011).
14. L. V. Wang and S. Hu, "Photoacoustic tomography: in vivo imaging from organelles to organs," *Science* **335**(6075), 1458–1462 (2012).
15. J. Liang et al., "Random-access optical-resolution photoacoustic microscopy using a digital micromirror device," *Opt. Lett.* **38**(15), 2683–2686 (2013).
16. P. Hai et al., "Near-infrared optical-resolution photoacoustic microscopy," *Opt. Lett.* **39**(17), 5192–5195 (2014).
17. J. Jose et al., "Imaging of tumor vasculature using Twente photoacoustic systems," *J. Biophotonics* **2**(12), 701–717 (2009).
18. G. Gao, S. Yang, and D. Xing, "Viscoelasticity imaging of biological tissues with phase-resolved photoacoustic measurement," *Opt. Lett.* **36**(17), 3341–3343 (2011).
19. A. Needles et al., "Development and initial application of a fully integrated photoacoustic micro-ultrasound system," *IEEE Trans. Ultrason. Ferroelectr. Freq. Control* **60**(5), 888–897 (2013).
20. Y. Zhou et al., "Handheld photoacoustic probe to detect both melanoma depth and volume at high speed in vivo," *J. Biophotonics* **8**(11–12), 961–967 (2015).
21. M. Xu and L. V. Wang, "Universal back-projection algorithm for photoacoustic computed tomography," *Phys. Rev. E.* **71**(1), 016706 (2005).
22. T. J. Hall et al., "Phantom materials for elastography," *IEEE Trans. Ultrason. Ferroelectr. Freq. Control* **44**(6), 1355–1365 (1997).
23. B. F. Kennedy et al., "In vivo dynamic optical coherence elastography using a ring actuator," *Opt. Express* **17**(24), 21762–21772 (2009).
24. L. V. Wang and L. Gao, "Photoacoustic microscopy and computed tomography: from bench to bedside," *Annu. Rev. Biomed. Eng.* **16**, 155–185 (2014).
25. Y. Zhou et al., "Calibration-free in vivo transverse blood flowmetry based on cross correlation of slow time profiles from photoacoustic microscopy," *Opt. Lett.* **38**(19), 3882–3885 (2013).
26. Y. Zhou et al., "Photoacoustic microscopy of bilirubin in tissue phantoms," *J. Biomed. Opt.* **17**(12), 126019 (2012).
27. H. F. Zhang et al., "Functional photoacoustic microscopy for high-resolution and noninvasive in vivo imaging," *Nat. Biotechnol.* **24**(7), 848–851 (2006).

Pengfei Hai is currently a PhD candidate in biomedical engineering at Washington University in St. Louis, under the supervision of Professor Lihong V. Wang. He received his BS degree in biomedical engineering from Shanghai Jiao Tong University in 2012. His research interests include the technical development and biomedical applications of photoacoustic imaging.

Yong Zhou is currently a graduate student in biomedical engineering at Washington University in St. Louis, under the supervision of Dr. Lihong V. Wang, Gene K. Beare distinguished professor. His research focuses on the development of photoacoustic imaging systems.

Jinyang Liang is currently a postdoctoral research associate in the Department of Biomedical Engineering at Washington University in St. Louis. His primary research focuses on the implementation of optical modulation techniques to develop modern optical instruments for applications in biology and physics. He received a PhD in electrical engineering from the University of Texas at Austin in 2012.

Chiye Li received his BS degree in life sciences from the University of Science and Technology of China, Hefei, China, in 2011. Currently, he is a PhD student in biomedical engineering at Washington University in St. Louis. His research interests involve the application of photoacoustic imaging techniques in biological and medical studies.

Lihong V. Wang is the Gene K. Beare distinguished professor at Washington University. He has published 437 journal articles (h-index=99, citations >39,000) and delivered 433 keynote, plenary, or invited talks. His laboratory published the first functional photoacoustic CT and three-dimensional photoacoustic microscopy. He received the Goodman Award for his *Biomedical Optics* textbook, NIH Director's Pioneer Award, OSA Mees Medal, IEEE Technical Achievement and Biomedical Engineering Awards, SPIE Britton Chance Biomedical Optics Award, and an honorary doctorate from Lund University, Sweden.